PHYSICAL REVIEW A **82**, 012506 (2010)

Dipole transition strengths in Ba$^+$ from Rydberg fine-structure measurements in Ba and Ba$^+$

Shannon L. Woods, M. E. Hanni, and S. R. Lundeen
Colorado State University, Fort Collins, Colorado 80523, USA

Erica L. Snow
State University of New York at Fredonia, Fredonia, New York 14063, USA

(Received 18 May 2010; published 12 July 2010)

The fine structure of high-L $n = 19$ and 20 Rydberg states of Ba$^+$ has been measured precisely using the resonant excitation Stark ionization spectroscopy technique, allowing for a determination of the Ba^{2+} polarizability: $\alpha_D(\text{Ba}^{2+}) = 10.75(10)$ a.u. This result, in combination with an improved model of the K splittings in Ba Rydberg levels, allows for a more precise determination of the Ba$^+$ dipole transition strengths connecting the $6\,^2S_{1/2}$ ground state to the $6\,^2P_{1/2}$ and $6\,^2P_{3/2}$ excited states. The results, in atomic units, are $\langle 6\,^2S_{1/2}\,||D||\,6\,^2P_{1/2}\rangle = 3.3251(21)$ and $\langle 6\,^2\text{S}_{1/2}\,||D||\,6\,^2P_{3/2}\rangle = 4.7017(27)$.

DOI: 10.1103/PhysRevA.82.012506 PACS number(s): 32.70.Cs, 32.10.Fn, 32.10.Dk

I. INTRODUCTION

Knowledge of atomic transition strengths is necessary for a wide range of atomic physics applications, from tests of fundamental interaction strengths to proposals for quantum computers and precise optical clocks. Since transition strengths are much more difficult to measure precisely than atomic and ionic binding energies, applications usually rely on theoretical calculations. The reliability of these calculations can only be established by experimental tests. Direct measurements of excited state lifetimes continue to provide such tests in a variety of atoms and ions [1]. For positive ions, a complementary tool is the study of fine-structure patterns in nonpenetrating Rydberg levels bound to the positive ion in question. These patterns depend on the properties of the positive ion that control its long-range interactions, such as dipole and quadrupole polarizabilities. In general, these properties depend on transition strengths connecting the ground state to all possible excited levels. In some cases, however, the transitions to the lowest excited states are dominant, allowing the Rydberg measurements to determine specific transition strengths. A good example is the recent study of transition strengths in the Ba$^+$ ion [2]. A measurement of that ion's dipole polarizability, obtained from study of fine-structure patterns in high-L barium Rydberg levels [3], was combined with measurements of K splittings in the same Rydberg levels [3] to infer transition strengths between the $6\,^2S_{1/2}$ ground state of Ba$^+$ and the two $6\,^2P$ excited levels. Both the dipole polarizability and the dipole contribution to the K splittings are almost entirely due to transitions to the $6\,^2P$ levels. An interesting feature of this study is the contrasting way in which contributions from the two $6\,^2P$ levels enter into the two measured features. The contributions to the dipole polarizability are directly additive,

$$\alpha_D\,(6P) = \frac{1}{3}\left[\frac{|\langle 6\,^2S_{1/2}\,\|D\|\,6\,^2P_{1/2}\rangle|^2}{E(6\,^2P_{1/2})} + \frac{|\langle 6\,^2S_{1/2}\,\|D\|\,6\,^2P_{3/2}\rangle|^2}{E(6\,^2P_{3/2})}\right], \tag{1}$$

while the contributions to the K splittings from these two excitations nearly cancel:

$$\delta E(6P) \cong \frac{(2L+1)\langle r^{-6}\rangle_{nL}}{12}\left[\frac{2|\langle 6\,^2S_{1/2}\,\|D\|\,6\,^2P_{1/2}\rangle|^2}{E(6\,^2P_{1/2})^2} - \frac{|\langle 6\,^2S_{1/2}\,\|D\|\,6\,^2P_{3/2}\rangle|^2}{E(6\,^2P_{3/2})^2}\right]. \tag{2}$$

Since the excitation energies of both states are precisely known, the combination of the two types of Rydberg measurement allows a determination of both matrix elements and their ratio.

The limiting factor in this previous study was the uncertainty in the polarizability of the Ba^{2+} core of the Ba$^+$ ion. The total calculated dipole polarizability of Ba$^+$ (124.15 a.u.) was given by Eq. (1) plus three additional contributions [4]:

(1) Higher excited levels (0.10 a.u.).
(2) A valence core correction (–0.51 a.u.).
(3) The core polarizability [10.61(53) a.u.].

Since the uncertainty in the measured dipole polarizability was only 0.05 a.u., the poorly known core polarizability limited the precision with which the dipole transition strengths could be extracted. That provided the motivation for the present study. We report here a new measurement of the dipole polarizability of Ba^{2+} obtained by the resonant excitation Stark ionization spectroscopy (RESIS) method. The result reduces this limiting uncertainty by a factor of five. In order to take full advantage of this improvement, some small additional terms in the theoretical description of the K splittings are also calculated. These two steps combine to improve the precision of transition strengths and their ratio to better than 0.1%.

II. SPECTROSCOPY OF RYDBERG LEVELS OF Ba$^+$

In order to determine the polarizability of Ba^{2+}, high-L Rydberg levels of the Ba$^+$ ion were studied using the RESIS technique. The method is similar to that used in a recent study of Rydberg levels of Pb$^+$ and Pb^{3+} [5]. A beam of Ba^{2+} ions was extracted from an electron cyclotron resonance (ECR) ion source and accelerated to approximately 20 keV. The mass selected ion beam passed through a dense Rb Rydberg target

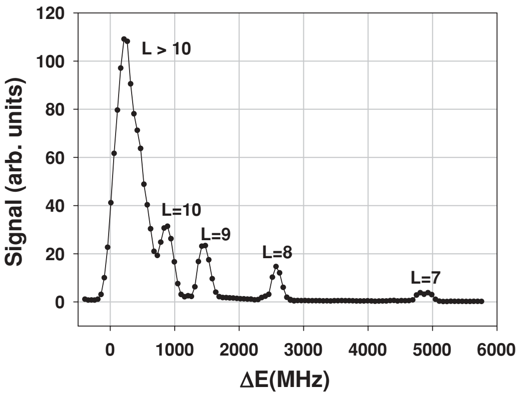

FIG. 1. Spectrum of $n = 19$ to $n' = 52$ RESIS excitations in Ba^+. The x axis is the difference of the Doppler-tuned laser frequency from the nonrelativistic hydrogenic frequency for the $(n,n') = (19,52)$ transition. The y axis is a measure of the flux of Ba^{2+} ions synchronous with the chopping frequency of the CO_2 laser. The large peak represents unresolved excitation of $n = 19$ levels with $L > 10$. The four resolved peaks at slightly higher frequencies represent excitation of $n = 19$ levels with the indicated L's.

where a small fraction of the ions (∼1%) captured an electron to form highly excited Rydberg Ba^+ ions. A charge-selection magnet rejected ions that had not captured an electron, and two einzel lenses focused the beam and ionized very weakly bound levels. The Rydberg ion beam then passed through a cw CO_2 laser whose fixed frequency was chosen to be close to that required to excite the ions from a populated level into a highly excited level. For this study, typical transitions were $(n,n') = (19,52)$ and $(20,52)$. Any ions excited to the upper level were Stark ionized, and the resulting Ba^{2+} ions were collected and counted. The CO_2 laser was Doppler tuned by changing the angle of intersection between the fast Rydberg ion beam and the laser. Figure 1 shows a typical spectrum of transitions observed in this way. The x axis shows the difference of the Doppler-tuned laser frequency from the nonrelativistic hydrogenic frequency for this transition. The y axis shows the Ba^{2+} ion current synchronous with chopping of the CO_2 laser. The large peak represents the unresolved excitation of the highest L levels of $n = 19$ while the four resolved peaks represent excitation of $n = 19$ levels with $L = 7$, 8, 9, and 10.

Extracting the transition frequencies from data such as in Fig. 1 relies upon knowledge of the fixed CO_2 laser frequency, the velocity of the Rydberg ion beam, and the angle of intersection of the laser with the ion beam. The laser frequencies have been precisely measured [6], and in this experiment their precision, estimated to be ±10 MHz, is limited by the degree to which the laser cavity length is stabilized to the peak of the laser gain curve. The ion beam velocity [$\beta = 0.000\,558\,7\,(5)$] is known to 0.1% from careful calibration of the acceleration voltage. The intersection angle, Θ_{int}, is controlled by a computer-driven rotation stage and is related by an arbitrary offset, $\Theta_\perp$, to the computer's setting, Θ_S:

$$\Theta_{\text{int}} = 90 - 2(\Theta_S - \Theta_\perp), \tag{3}$$

where $\Theta_\perp$ is the stage angle at which the laser intersects the ion beam at an angle of 90°. The value of $\Theta_\perp$, $1.09(3)^\circ$, was found by observing a fine-structure pattern of known scale [7].

TABLE I. Summary of the frequencies of the Ba^+ RESIS transitions observed in this study. Column 1 identifies the transition, and the number of observations is shown in column 2. Column 3 shows the measured difference of the transition frequency from the nonrelativistic hydrogenic transition frequency for the corresponding pair of principle quantum numbers. The uncertainty shown combines the statistical errors from fitting the data and estimating the Stark shift correction. Column 4 reports the estimated Stark shift of the transition, applied as a correction to arrive at the transition frequency reported in column 3.

Transition	N	ΔE (MHz)	ΔE_{Stark} (MHz)
(20,5)–(54,6)	3	21481(36)	−52(35)
(20,6)–(51,7)	2	8876(21)	−18(7)
(20,7)–(52,8)	5	4231(9)	7
(20,8)–(52,9)	5	2225(19)	3
(20,9)–(52,10)	5	1260(16)	1
(19,5)–(50,6)	3	24902(4)	−2(4)
(19,6)–(42,7)	2	10050(14)	−9(14)
(19,7)–(52,8)	2	4956(23)	1
(19,8)–(52,9)	2	2603(9)	2
(19,9)–(52,10)	2	1475(8)	1
(19,10)–(52,11)	2	880(8)	0

The Doppler-tuned laser frequency is given by

$$\upsilon_L' = \upsilon_L \frac{(1 + \beta \cos \Theta_{\text{int}})}{\sqrt{1 - \beta^2}}. \tag{4}$$

Each transition frequency differs only slightly from the nonrelativistic transition frequency corresponding to the principle quantum numbers for the transition (n,n'). Therefore, only the frequency difference is reported in Table I for the eleven transitions measured in this study.

A significant experimental issue is the possible Stark shift of the transitions due to stray electric fields in the laser interaction region. These were estimated and applied as corrections using two different methods. For the $L \geqslant 7$ initial states, where the upper state of the transition was imbedded closely in the Stark manifold, a simulation program diagonalized the Stark Hamiltonian to predict the width and shift of the Stark broadened line shape as a function of the stray field. The observed width of the experimental lines was then used to estimate the stray field and determine a Stark shift correction. Typical values of the stray field were less than 0.05 V/cm. The resulting Stark shifts were quite small because of the compensating effects of the downward Stark shift of the nominal final state and the additional transition strength to higher energy levels allowed because of the Stark mixture. The transitions from $L < 7$ initial states go to upper states that are well resolved from the Stark manifold. In these cases, the Stark-allowed $\Delta L = 2$ or $\Delta L = 0$ transitions were visible, giving convenient measures of the stray field. The Stark shift correction was estimated using the calculated quadratic Stark shift rate of the nominal upper state. Table I lists the estimated Stark shifts of all the transitions studied. The reported frequency offsets, ΔE_{obs}, have been corrected for these shifts. The uncertainties shown in Table I do not include the systematic uncertainties in β or $\Theta_\perp$.

TABLE II. Summary of scaled frequency offsets, after correction for relativistic and second-order polarization energies. Column 1 gives the transition; columns 2 and 3 report the relativistic and second-order contributions to the observed frequency offset from hydrogenic. Column 4 shows the corrected frequency offset scaled by the difference of expectation values of r^{-4} in the upper and lower levels of the transition. Column 5 shows the ratio of the difference of r^{-6} and r^{-4} expectation values. Columns 4 and 5, in which both numerator and denominator are expressed in atomic units, become the *y* and *x* coordinates in Fig. 2.

Transition	$\Delta E^{\rm rel}$ (MHz)	$\Delta E^{[2]}$ (MHz)	$\frac{\Delta E_{\rm obs} - \Delta E^{\rm rel} - \Delta E^{[2]}}{\Delta\langle r^{-4}\rangle}$	$\frac{\Delta\langle r^{-6}\rangle}{\Delta\langle r^{-4}\rangle}$ (units of 10^3)
(20,5)–(54,6)	48	255	5.432(9)	15.445
(20,6)–51,7)	38	38	5.364(13)	7.309
(20,7)–(52,8)	32	7	5.329(11)	3.878
(20,8)–(52,9)	26	2	5.338(46)	2.233
(20,9)–(52,10)	22	1	5.363(72)	1.365
(19,5)–(50,6)	55	297	5.424(1)	15.392
(19,6)–(42,7)	42	43	5.317(8)	7.316
(19,7)–(52,8)	36	9	5.365(25)	3.837
(19,8)–(52,9)	30	2	5.371(18)	2.203
(19,9)–(52,10)	25	1	5.407(29)	1.341
(19,10)–(52,11)	21	0	5.422(51)	0.853

In order to extract a value of the Ba^{2+} polarizability from these spectral measurements, they are compared with the predictions of the effective potential model [8,9]. This model describes the fine structure pattern in nonpenetrating high-L Rydberg states in terms of an effective potential seen by the Rydberg electron in addition to the dominant Coulomb attraction of the core ion. Since Ba^{2+} has a $^1S_0$ ground state, the effective potential contains only scalar terms and is of the form

$$V_{\rm eff} = -\frac{\alpha_D}{2r^4} - \frac{(\alpha_Q - 6\beta_D)}{2r^6} + \cdots, \quad (5)$$

where the coefficients are properties of the core ion: α_D, the total dipole polarizability; α_Q, the quadrupole polarizability; and β_D, the nonadiabatic dipole polarizability. The energy levels can then be expressed in terms of $V_{\rm eff}$ by

$$E(nL) = E^0(n) + E^{\rm rel}(nL) + E^{[1]}(nL) + E^{[2]}(nL), \quad (6)$$

where $E^0(n)$ is the zeroth-order energy of a Rydberg level with principle quantum number n. The second term, $E^{\rm rel}$, is a relativistic correction due to the p^4 contributions to kinetic energy and is given by

$$E^{\rm rel} = \frac{\alpha^2 Q^4}{2n^4}\left[\frac{3}{4} - \frac{n}{L + (1/2)}\right]. \quad (7)$$

The third term, $E^{[1]}(nL)$, is the expectation value of $V_{\rm eff}$ and is by far the most significant contribution to the fine-structure pattern. The fourth term, $E^{[2]}(nL)$, comes from application of $V_{\rm eff}$ in second order and has been calculated analytically by Drake and Swainson [10] in the approximation that only the term proportional to α_D^2 is significant.

The relatively small contributions to the measured frequency offsets from $E^{\rm rel}$ and $E^{[2]}$ can be calculated and subtracted from the measured offsets to form a quantity that should scale simply with the radial expectation values in the relevant states. Specifically, we expect

$$\Delta E_{\rm obs} - \Delta E^{\rm rel} - \Delta E^{[2]} = \frac{\alpha_D}{2}\Delta\langle r^{-4}\rangle_{nL} + \frac{(\alpha_Q - 6\beta_D)}{2}\Delta\langle r^{-6}\rangle_{nL} + \cdots, \quad (8)$$

where $\Delta\langle r^{-4}\rangle_{nL}$ and so on is the difference of expectation values of r^{-4} in the upper and lower states of the transition. The relevant expectation values for hydrogenic radial wave functions are tabulated by Bockasten [11] but should be corrected for the reduced mass of the Ba^{2+} ion. As Table II shows, dividing the corrected frequency offsets by $\Delta\langle r^{-4}\rangle_{nL}$ removes nearly all the variation. When this scaled frequency offset is plotted as a function of the ratio of $\Delta\langle r^{-6}\rangle_{nL}$ to $\Delta\langle r^{-4}\rangle_{nL}$, as in Fig. 2, a linear extrapolation can be used to extract a value for the dipole polarizability. Figure 2 shows that the transitions from initial states with $L > 5$ are consistent with the expectation of a linear fit. The solid line in Fig. 2 corresponds to a linear fit of these points, giving an intercept that indicates

$$\alpha_D = 10.75(10) \text{ a.u.}$$

The corresponding intercept is shown in Fig. 2 as a solid square. The uncertainty in this result is due both to the statistical uncertainties in the interval measurements, from Table I, and to the systematic uncertainties in β and $\Theta_\perp$. The two transitions corresponding to $L = 5$ initial states deviate from the linear trend. This could indicate the importance of higher terms in the effective potential proportional to higher inverse powers of r. An alternate fit including the $L = 5$ points, but also including possible contributions proportional to r^{-8}, is indicated by the dashed line. Note that the intercept from this alternate fit is consistent with the result obtained.

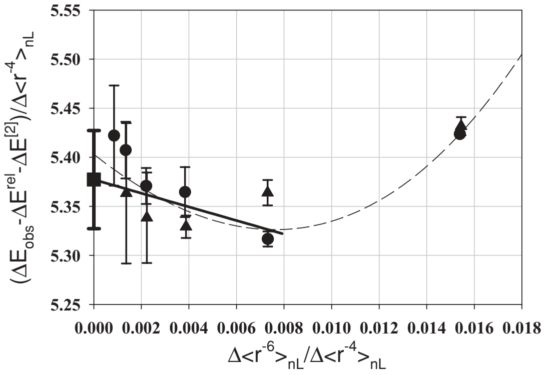

FIG. 2. Intervals corrected for relativistic and second-order energies and normalized to $\Delta\langle r^{-4}\rangle_{nL}$ are plotted as a function of $\Delta\langle r^{-6}\rangle_{nL}/\Delta\langle r^{-4}\rangle_{nL}$. The circles correspond to transitions from $n = 19$ levels, while the triangles correspond to transitions from $n = 20$ levels. The solid line is the result of a linear fit of the $L > 5$ data points. The intercept from this fit, shown by the solid square, determines the Ba^{2+} dipole polarizability. An alternate fit, including the $L = 5$ points and possible contributions proportional to r^{-8}, is shown by the dashed line. It finds an intercept consistent with the linear fit.

III. Ba *K* SPLITTINGS

If the barium Rydberg levels consisting of a single (n,L) Rydberg electron bound to the $^2S_{1/2}$ ground state of Ba^+ were adequately described by the adiabatic polarization model, the energy levels corresponding to the two possible values of the intermediate quantum number

$$\vec{K} = \vec{L} + \vec{J}_c \tag{9}$$

would be expected to be degenerate except for small magnetic effects. The first observations of such levels [12] showed clearly that this was not the case. Some years later, the physical origin of these anomalously large level splittings was traced to the influence of nonadiabatic corrections to the Rydberg fine structure, which introduces K splittings in the Rydberg levels proportional to the fine-structure splittings in the excited levels of the Ba^+ ion [13]. The Rydberg fine-structure energies and the related K splittings are dominated by the second-order perturbation energies with contributions from all multipole orders, but the K splittings vanish identically if the core excitation energies are large enough so that the adiabatic approximation is valid [2]. More generally, the perturbation energies can be expanded in a sequence of nonadiabatic corrections that give nonzero values of the K splittings. For example, Eq. (2) is an approximate expression for the contribution to the K splitting in the (n,L) Rydberg level from the first nonadiabatic correction to the second-order dipole perturbation energy.

Once the origin of these K splittings was understood, it was suggested that observations of K splittings could provide experimental measurements of transition strengths [14]. Equation (2) illustrates one potential advantage in this suggestion. Due to the presence of two powers of the excitation energy in the denominator, contributions to the K splittings are very heavily weighted toward the lowest excited levels of the ion. In barium, for example, only the $6p$ and $5d$ levels contribute significantly. Unfortunately, the initial estimates of Ba^+ transition strengths from K splittings were only partially successful because significant contributions from third- and fourth-order perturbation energies were neglected. Inclusion of these terms by Woods *et al.* [2] resolved previous discrepancies with calculated quadrupole transition strengths and provided measurements of both dipole matrix elements in Eq. (2). These measurements can be improved now that the Ba^{2+} dipole polarizability has been measured.

TABLE III. Calculated electric dipole and quadrupole matrix elements between the lowest five levels of the Ba^+ ion, from Ref. [4] and Ref. [16]. All values are in atomic units.

Quantity	Value
$\langle 6\,S_{1/2}\,\|D\|6\,P_{1/2}\rangle$	3.3357
$\langle 6\,S_{1/2}\,\|D\|6\,P_{3/2}\rangle$	4.7065
$\langle 6\,S_{1/2}\,\|Q\|5\,D_{3/2}\rangle$	−12.63(9)
$\langle 6\,S_{1/2}\,\|Q\|5\,D_{5/2}\rangle$	−15.8(1)
$\langle 6\,P_{1/2}\,\|D\|5\,D_{3/2}\rangle$	−3.034
$\langle 6\,P_{3/2}\,\|D\|5\,D_{3/2}\rangle$	−1.325
$\langle 6\,P_{3/2}\,\|D\|5\,D_{5/2}\rangle$	−4.080
$\langle 6\,P_{1/2}\,\|Q\|6\,P_{3/2}\rangle$	28.34
$\langle 6\,P_{3/2}\,\|Q\|6\,P_{3/2}\rangle$	−29.23

To take full advantage of the increased precision made possible by the Ba^{2+} polarizability measurement, the theoretical model used to calculate the K splittings [2] has been extended to include some smaller, calculable terms in the third- and fourth-order perturbation contributions to the K splittings. As described in Ref. [2], the theoretical model assumes the known values of the Ba^+ excited-state energies [15] and matrix elements calculated elsewhere using relativistic many-body perturbation theory [4,16]. The necessary matrix elements are shown in Table III. The only significant second-order contributions to the K splittings, denoted *DD* and *QQ* in Ref. [2], were calculated without recourse to the adiabatic expansion, using the Dalgarno-Lewis method to implicitly include contributions from both bound and continuum Rydberg levels. The results are shown in Table V of Ref. [2]. For this work, the contributions from third- and fourth-order perturbation terms were calculated somewhat more precisely than in Ref. [2] by including the first nonadiabatic correction to sums that involve an intermediate $6p$ core level. This is justified by the expected convergence of the adiabatic expansion because of the relatively high excitation energy of the $6p$ level. Table IV illustrates the new terms and the revised totals. As expected, the first nonadiabatic terms contribute less than 10% of the total third- and fourth-order contribution in all cases. The next nonadiabatic term, neglected here, would be expected to be less by another factor of order 10. The total uncertainty in the calculated third- and fourth-order contributions is estimated to be about 5%. This includes errors due to neglected terms in the adiabatic or perturbation expansion and additional uncertainties due to possible inaccuracies of the matrix elements assumed for the calculations.

Table V shows the measured K splittings in $n = 17$ and $n = 20$ of Ba, as reported by Snow *et al.* [3]. As discussed in Ref. [2], the reported intervals, in particular the highest

TABLE IV. Additional third- and fourth-order contributions and revised totals. All values are in MHz.

(n,L)	$\delta E^{[3]}_{\mathrm{NEW}}$	$\delta E^{[3]}_{\mathrm{TOT}}$	$\delta E^{[4]}_{\mathrm{NEW}}$	$\delta E^{[4]}_{\mathrm{TOT}}$
(17,6)	−10.81	−185.23	−3.07	20.26
(17,7)	−0.58	−7.96	−0.15	0.63
(20,7)	−0.41	−5.55	−0.11	0.44
(17,8)	−0.09	−0.99	−0.01	0.06
(20,8)	−0.06	−0.70	−0.01	0.04
(7,9)	−0.01	−0.17	−0.00	0.01
(20,9)	−0.01	−0.12	−0.00	0.01

L splittings, are influenced by differential Stark shifts that were not considered in Ref. [3]. The splittings reported in column 3 of Table V have been corrected for these differential shifts, using $f_S = 0.13(4)$, as determined in Ref. [2]. The measured splittings in levels with $L = 10$ and 11 are not included in Table V because their precision is not sufficient to affect the subsequent discussion. Table V also shows the theoretical predictions of the K splittings, calculated with the model described previously. These are formed by adding the DD and QQ terms listed in Ref. [2] to the revised third- and fourth-order contributions shown in Table IV. The theoretical uncertainties shown correspond to the 5% uncertainty in the calculated third- and fourth-order contributions. The fifth column of Table V shows the ratio between the measured K splittings, corrected for differential Stark shifts, and the theoretical calculation. Although the agreement is within a few percentage points in each case, there is a clear trend showing systematic deviation from the calculations. This is illustrated in Fig. 3(a), which plots the ratio versus L. In general, the calculated splittings are too small at lower L and too large at higher L.

The disagreement between measured and calculated K splittings illustrated in Fig. 3 is likely due to inaccuracy of the first four matrix elements listed in Table III, the dipole and quadrupole matrix elements connecting the ground state to the 6p and 5d levels. The only other experimental tests of these matrix elements, obtained from excited-state lifetime measurements, do not rule out errors on the order of a few percentage points. The implications of the K splitting measurements for these matrix elements can be explored by modifying the DD and QQ contributions to the splittings by variable factors:

$$\delta E_T \Rightarrow A_1 \delta E_{DD} + A_2 \delta E_{QQ} + (\delta E^{[3]} + \delta E^{[4]}).$$

This modification results in an excellent fit to the data. Figure 3b shows the effect of allowing the coefficients A_1 and A_2 to differ from 1. The quadrupole contribution is slightly increased to match the decreasing trend versus L, and the dipole contribution is slightly decreased to compensate at high L. The parameters returned by this fit are

$$A_1 = 0.969(9),$$
$$A_2 = 1.056(23).$$

The last column of Table V shows the improved agreement between the measured splittings and the predictions using the fitted values of A_1 and A_2. The fitted parameters A_1 and A_2 are very similar to the factors found in Ref. [2]. The most significant difference is in the parameter A_2, but the change is not sufficient to significantly alter the conclusions of Ref. [2] regarding the quadrupole transition strengths.

The required −3.1(9)% modification of the DD contribution to the K splittings places a strict limit on the ratio of the two dipole matrix elements connecting the $6\,^2S_{1/2}$ ground state of Ba$^+$ to the $6\,^2P_{1/2}$ and $6\,^2P_{3/2}$ excited states. This is due to the near cancellation illustrated in Eq. (2), which enhances the fractional effect of a change in the matrix element ratio.

TABLE V. Comparison between measured K splittings in $n = 17$ and 20 Rydberg levels of Ba with theoretical calculations. Column 1 identifies the level where the K splitting was observed; column 2 shows the interval reported in Ref. [3]. Column 3 shows the corrected interval after accounting for the differential Stark shift discussed in Ref. [2]. Column 4 shows the total calculated splitting, using the model described in the text and the calculated matrix elements listed in Table III. All values are in MHz. Column 5 shows the ratio between the observed splittings (as corrected) and the total theoretical prediction of column 4. Column 6 shows the same ratio after adjusting the theoretical predictions by the factors A_1 and A_2, as discussed in the text.

(n,L)	δE–δE_N	δE–δE_N–$\delta E_{\mathrm{Stark}}$	$\delta E_{\mathrm{Theory}}$	$\dfrac{\delta E_{\mathrm{obs}} - \delta E_N - \delta E_{\mathrm{Stark}}}{\delta E_{\mathrm{Theory}}}$	$\dfrac{\delta E_{\mathrm{obs}} - \delta E_N - \delta E_{\mathrm{Stark}}}{\delta E'_{\mathrm{Theory}}}$
(17,6)	263.37(10)	263.37(10)	254.63(825)	1.034(32)	0.980(32)
(17,7)	41.95(9)	41.96(9)	41.78(37)	1.004(9)	1.008(9)
(20,7)	27.33(6)	27.35(6)	27.35(26)	1.000(10)	1.002(10)
(17,8)	13.03(11)	13.06(11)	13.21(5)	0.988(9)	1.005(9)
(20,8)	8.45(5)	8.52(5)	8.72(3)	0.977(7)	0.993(7)
(17,9)	4.76(12)	4.81(12)	4.89(1)	0.984(25)	1.006(25)
(20,9)	2.95(13)	3.10(14)	3.29(1)	0.942(42)	0.964(42)

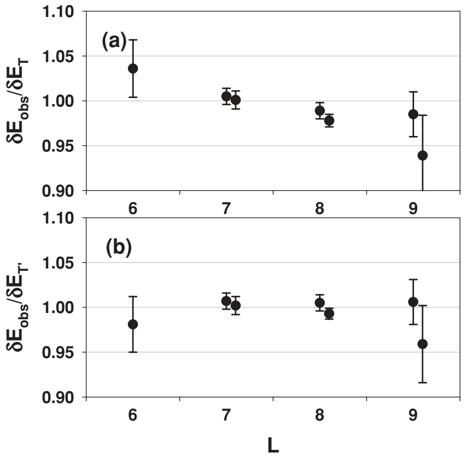

FIG. 3. (a) Comparison between observed K splittings and the values calculated using the known term values and the matrix elements listed in Table III. The vertical axis shows the ratio, from column 5 of Table V. A systematic deviation is indicated by the downward slope vs L. (b) The same plot after correcting the theoretical predictions by the factors A_1 and A_2. The vertical axis shows the revised ratios, from column 6 of Table V.

For example, a change in the matrix element ratio by 0.10% changes the result of Eq. (2) by 1.2%, an enhancement by more than an order of magnitude. Although Eq. (2) does not accurately represent the DD contribution to the K splittings, it does serve to illustrate the extreme sensitivity of the K splitting measurements to the matrix element ratio. There is, of course, no particular sensitivity to the magnitude of either matrix element in the K splitting data, but fortunately the precise measurement (0.04%) of the dipole polarizability of Ba$^+$ [3] sets a tight limit on this. As Eq. (1) illustrates, the polarizability is directly sensitive to the matrix element magnitude while being nearly insensitive to the ratio between matrix elements. The combined restrictions posed by these two complementary measurements are illustrated in Fig. 4. The horizontal and vertical axes show the square of the two dipole matrix elements. The calculated matrix elements from Table III are illustrated by the open square. The restriction posed by the K splitting measurements on the matrix element ratio is illustrated by the two solid upward-sloping lines. The complementary restriction posed by the polarizability measurement is illustrated by the downward-sloping solid lines. This restriction is significantly tighter than reported in Ref. [2] because it is no longer limited by the estimated theoretical uncertainty in the Ba^{2+} polarizability. The intersection of these two defines the solid ellipse, showing the range of matrix elements consistent with both. The resulting determinations of both matrix elements are shown in Table VI. Each matrix element is determined in this way with precision of better than 0.1%, and both agree with the calculated matrix elements of Table III to within a few tenths of a percentage point. The ratio between the two matrix elements is determined in this way to better than 0.1%. The result is completely consistent with the ratio expected for pure LS coupling, illustrated by the dotted line in Fig. 4, but inconsistent with the 0.23% deviation from the LS coupling ratio found in the calculated matrix elements of Table III.

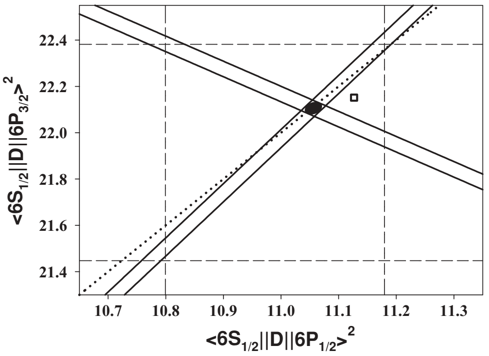

FIG. 4. Square of the dipole matrix elements connecting the Ba$^+$ ground state to the excited 6 $P_{1/2}$ state (horizontal axis) and the 6 $P_{3/2}$ state (vertical axis). The open square shows the theoretical matrix elements from Table V while the dotted line represents the values of the matrix elements consistent with LS coupling. The dashed lines are from the measured lifetimes [17]. The upward-sloping solid lines are due to the K splittings while the downward-sloping lines result from the dipole polarizability [3].

Figure 4 also illustrates, for comparison, the limits on the two transition strengths posed by measurements of the 6p lifetimes [17]. Because the 6p decay has two branches (6s, 5d), the lifetime measurements do not immediately imply values of the 6s–6p matrix elements. The values illustrated in Fig. 4 assume that the 6p–5d matrix elements in Table III are accurate and calculate the implied 6s–6p matrix elements using the expressions in the appendix to Ref. [2]. The approximately 1% precision of the lifetime measurements of Ref. [17] are typical of the fast beam laser lifetime measurements, which have produced the recent most precise values. Reference [18] reports similar measurements and includes a comparison with results obtained using older methods. One unusually precise (0.25%) measurement of the 6 $P_{3/2}$ lifetime by the fast beam laser technique [19] can be combined with our measurement of the 6 $S_{1/2}$–6 $P_{3/2}$ matrix element to determine the 6 $P_{3/2}$ to 5d transition probability. The result is 2.1(1.0)% lower than the value implied by the matrix elements of Table III, confirming those calculated matrix elements at the level of about 1%. Another interesting, but so far less precise, technique determines specific transition probabilities by measuring optical nutation frequencies on laser-induced transitions in Ba$^+$ [20]. A more extensive compilation of both experimental and theoretical estimates of transition probabilities is available at the National Institute of Standards and Technology Atomic Transition Probability Bibliographic Database [21].

TABLE VI. Limits on the electric dipole matrix elements and their ratios derived from the K splitting and polarizability measurements in barium Rydberg levels. All values are in atomic units.

Quantity	Expt.	(Expt.)/(Theory)
$\langle 6\,S_{1/2}\,\|D\|6P_{1/2}\rangle$	3.3251(21)	0.9968(6)
$\langle 6\,S_{1/2}\,\|D\|6P_{3/2}\rangle$	4.7017(27)	0.9990(6)
Ratio	0.7072(6)	0.9978(8)

IV. CONCLUSIONS

The polarizability of Ba^{2+} has been measured with 1% precision by the RESIS method. This reduces the primary source of uncertainty in the theoretical calculation of the Ba$^+$ polarizability. Combining the previously reported measurements of fine structure and K splittings in high-L Rydberg levels of Ba leads to 0.1% determinations of both dipole matrix elements connecting the $6\,^2S_{1/2}$ ground state of Ba$^+$ to the $6\,^2P$ levels. The results agree to within a few tenths of a percentage point with calculations that use relativistic many-body perturbation theory. The high precision of the experimental results suggests that measurements of K splittings and Rydberg fine-structure patterns in Rydberg levels of other atoms and ions could provide additional valuable tests of atomic calculations in those systems. Among the systems where such data would be especially valuable are the ions Ca$^+$, Sr$^+$, Hg$^+$, and Yb$^+$, which are candidates for precise optical-frequency standards and where reliable measurements of ground-state polarizabilities are needed. However, similar measurements could be useful in a much wider range of positive ions.

ACKNOWLEDGMENTS

We thank Marianna Safronova for providing results of unpublished work and Charles Fehrenbach for assistance with the experimental measurements. This work was supported by the Chemical Sciences, Geosciences, and Biosciences Division of the Office of Basic Energy Sciences, Office of Science, US Department of Energy.

---

[1] R. E. Imhof and R. H. Read, Rep. Prog. Phys. **40**, 1 (1977).

[2] S. L. Woods, S. R. Lundeen, and E. L. Snow, Phys. Rev. A **80**, 042516 (2009).

[3] E. L. Snow and S. R. Lundeen, Phys. Rev. A **76**, 052505 (2007).

[4] E. Iskrenova-Tchoukova and M. S. Safronova, Phys. Rev. A **78**, 012508 (2008).

[5] M. E. Hanni, J. A. Keele, S. R. Lundeen, C. W. Fehrenbach, and W. G. Sturrus, Phys. Rev. A **81**, 042512 (2010).

[6] M. J. Weber, ed., *Handbook of Laser Science and Technology* (CRC Press, Boca Raton, FL, 1982), Vol. 2.

[7] R. A. Komara, M. A. Gearba, S. R. Lundeen, and C. W. Fehrenbach, Phys. Rev. A **67**, 062502 (2003).

[8] B. Edlén, *Handbuch der Physik XXVII*, edited by S. Flügge (Springer-Verlag, Berlin, 1964), pp. 80–220.

[9] R. J. Drachman, Phys. Rev. A **26**, 1228 (1982).

[10] G. W. F. Drake and R. A. Swainson, Phys. Rev. A **44**, 5448 (1991).

[11] K. Bockasten, Phys. Rev. A **9**, 1087 (1974).

[12] T. F. Gallagher, R. Kachru, and N. H. Tran, Phys. Rev. A **26**, 2611 (1982).

[13] E. L. Snow, R. A. Komara, M. A. Gearba, and S. R. Lundeen, Phys. Rev. A **68**, 022510 (2003).

[14] E. S. Shuman and T. F. Gallagher, Phys. Rev. A **74**, 022502 (2006).

[15] Y. Ralchenko, A. E. Kramida, J. Reader, and NIST ASD Team, NIST Atomic Spectra Database (version 3.1.5), [physics.nist.gov/asd3].

[16] M. S. Safronova (private communication).

[17] E. H. Pinnington, R. W. Berends, and M. Lumsden, J. Phys. B: At. Mol. Opt. Phys. **28**, 2095 (1995) (6 $P_{1/2}$ and 6 $P_{3/2}$).

[18] P. Kuske, N. Kirchner, W. Wittmann, H. J. Andrä, and D. Kaiser, Phys. Lett. A **64**, 377 (1978).

[19] H. J. Andrä, in *Beam-Foil Spectroscopy*, edited by I. A. Sellin and D. J. Pegg (Plenum, New York, 1976), Vol. 2, p. 835.

[20] A. Kastberg, P. Villemoes, A. Arnesen, F. Heijkenskjöld, A. Langereis, P. Jungner, and S. Linnaeus, J. Opt. Soc. Am. B **10**, 1330 (1993).

[21] J. R. Fuhr, A. E. Kramida, H. R. Felrice, K. Olsen, and S. Kotochigova, NIST Atomic Transition Probability Bibliographic Database (version 8.1), [physics.nist.gov/cgi-bin/ASBib1/TransProbBib.cgi].